Astrochemistry in the Laboratory
REU Program at Columbia University - Nevis Laboratories

Ash Bista[1]

[1]Rochester Institute of Technology

August 2, 2023

Contents

1 Abstract

Stars and their pathway to planetary systems contain the secrets of our cosmic origins. In order to observe the stellar evolutionary track, we analyze chemical information encoded in the emissions of organic molecules surrounding prestellar cores and protoplanetary disks. Of particular interest is $N2_H^+$ (and $N2_D^+$) as we can answer questions about the reactions that occur in these stellar objects that lead to these ions, observed abundance ratios being orders of magnitudes above the Big Bang Nucleosynthesis-created galactic D/H ratio, the implications of chemical ages giving longer timescales than current astrochemical models predict for core formation, the role of magnetic fields in this process, and tracer densities or other stellar properties that impact our understanding of disk structures. However, this hinges on accurate kinetics data, which is currently lacking as thermal rate coefficients scatter by a factor of 2 and do not agree within error. We aim to provide reliable kinetics data by reacting N_2 with H_3^+ (and its isotopologues) to produce $N2_H^+$ (and $N2_D^+$) and making measurements using our dual-source ion-neutral merged-fast-beam apparatus. Preparatory hardware work was involved in order to run the necessary experiments, which was my specific role in the project.

2 Introduction

Our overarching scientific goal is to study the formation, evolution, and function of stars. Along the pathway of stellar evolution are prestellar cores and protoplanetary disks which we aim to provide a deeper look into with measurements of reaction cross sections, as is necessary for the study of deuterium fractionation, abundance ratios, chemical ages, magnetic fields, tracer densities, stellar properties (i.e. temperature, thermal history, ionization fraction, and chemical composition), and structures of these objects. Specifically we look at (N_2) reacting with tritium (H_3^+). which results in daughter ion products, N_2H^+ and N_2D^+, that are used as tracers for the desired characteristics mentioned above. The following is a review of the current knowledge on this topic.

2.1 Background & Motivation

The Universe begins with a bang. Here, it releases hydrogen, helium, and trace amounts of lithium, beryllium, and boron, the foundational elements upon which all other matter in the world is created from. This is where the stars come in to play and shine in their essential role; most simply put, stars are nature's chemical factories. They fuse hydrogen into helium, and then through nucleosynthesis form carbon, oxygen, and other heavier elements. Everything, yourself included, is made of star-stuff.

2.1.1 Star Formation

How do stars form? Starting with the first stars, whose core-created elements eject into space and interact with the gas and dust of the interstellar medium (ISM), gives rise to generations of new stars where the cycle of creation and destruction repeat. "Stellar nurseries"/"star-forming regions" are a way to refer to diffuse nebulae, formed from the collapse of low density diffuse clouds in the ISM into dense clouds in which atomic hydrogen becomes molecular hydrogen, hence the name molecular clouds. A molecular cloud overcomes equilibrium and continues to undergo gravitational collapse due to triggers such as collisions with other clouds, high velocity shocked matter from supernova explosions, and radio emissions around ejected material (jets) in supermassive black holes, or from starbursts when the tidal forces in galactic collisions compress and agitate gas. In the collapsing

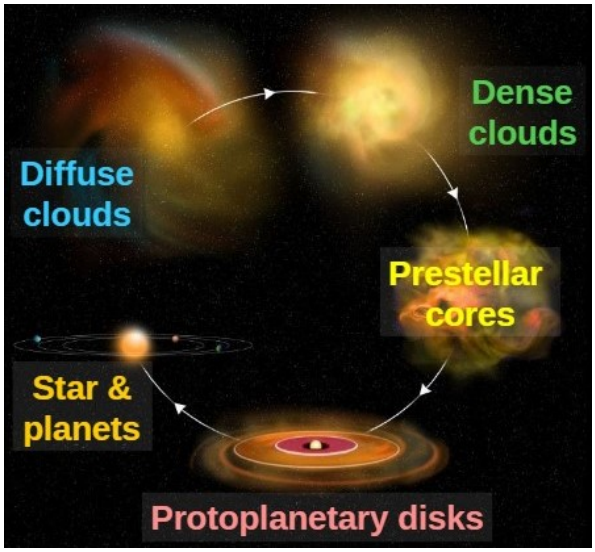

Figure 1: *Life Cycle of a Star. Credit: Bill Saxton, NRAO/AUI/NSF.*

process, the molecular cloud will hierarchically break apart into smaller pieces through the effects of turbulence, macroscopic flows, rotation, magnetic fields and the cloud geometry [12]. Cloud fragments will radiate away energy until they are opaque enough from an increased density, and the raised temperatures in the cloud further fragmentation, causing fragments to condense and become small rotating spheres of gas or "stellar embryos" with a reservoir of accreted material orbiting them as a disk (see Figure 1 above). At a high enough temperature, the gas is ionized and turns the cloud transparent once again, and it's internal thermal pressure is now sufficient to halt collapse. A protostar is born. For the next hundreds of thousands of years it will gather mass from its parent cloud until the disk is cleared away and hydrogen fusion begins. This marks the end of the protostellar phase and it is now considered a main-sequence star.

2.1.2 Stellar Evolution

Once a star is formed, it will live on for millions to billions of years. This is due to the massive energy reserve they hold that needs to be expelled. Main sequence stars are powered by nuclear fusion in their cores of hydrogen into helium. This process enables the stars to grow in size since the core contracts and increases temperature, causing the outer layers to expand and cool. Eventually the star evolves off from the main sequence and follows the red giant branch on the Hertzsprung-Russell diagram [5] depicted in Figure 2 below. Once a star reaches approximately 3×10^8 K, cooling halts as it begins to fuse helium in the core, fuse hydrogen in concentric shells surrounding the center, and travels along the horizontal branch. Then helium fusion also depletes and the star returns to cooling and expanding as before, only now it is on the asymptotic giant branch. Here it has a core of heavy elements such as oxygen and carbon, and concentric shells of helium and hydrogen. Finally, the star will completely exhaust its nuclear fuel and undergo core collapse into a dense white dwarf. In this process its outer envelope is expelled as a planetary nebula. If a star is massive enough at this point it will instead explode as a supernova and the core will collapse into an extremely dense neutron star or even a black hole.

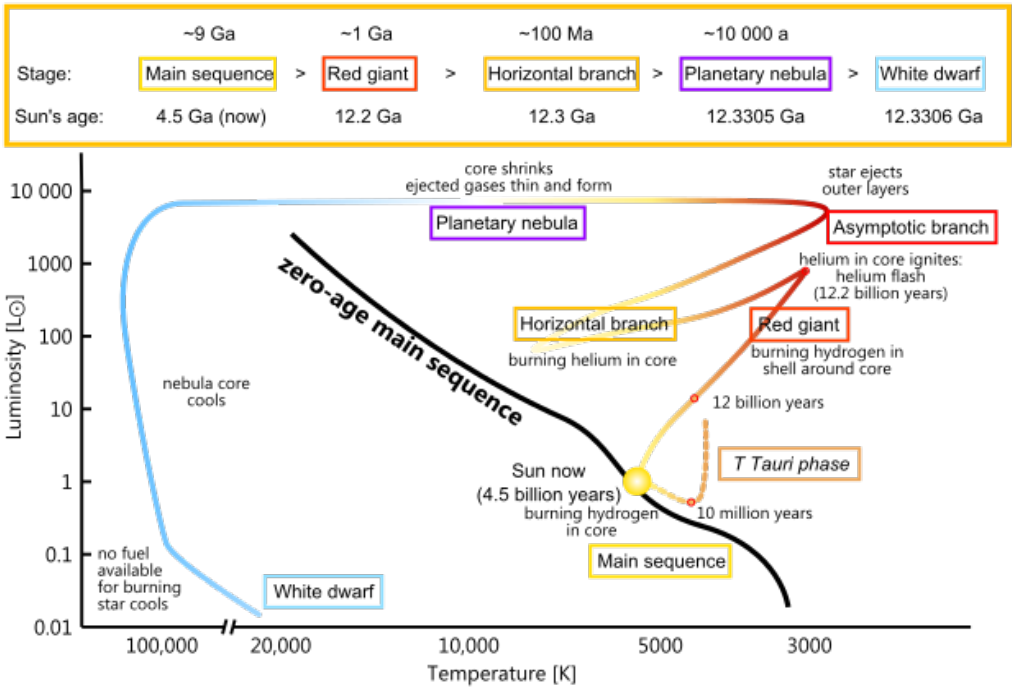

Figure 2: *Hertzsprung–Russell diagram showing the evolutionary track of a stellar object. Credit: NASA/CXC/SAO.*

2.2 Literature Review

Since stellar evolution is too long for us to observe as a whole, scientists observe stars at their different stages and make mathematical models to compare predictions with observations.

2.2.1 Deuterated Chemistry

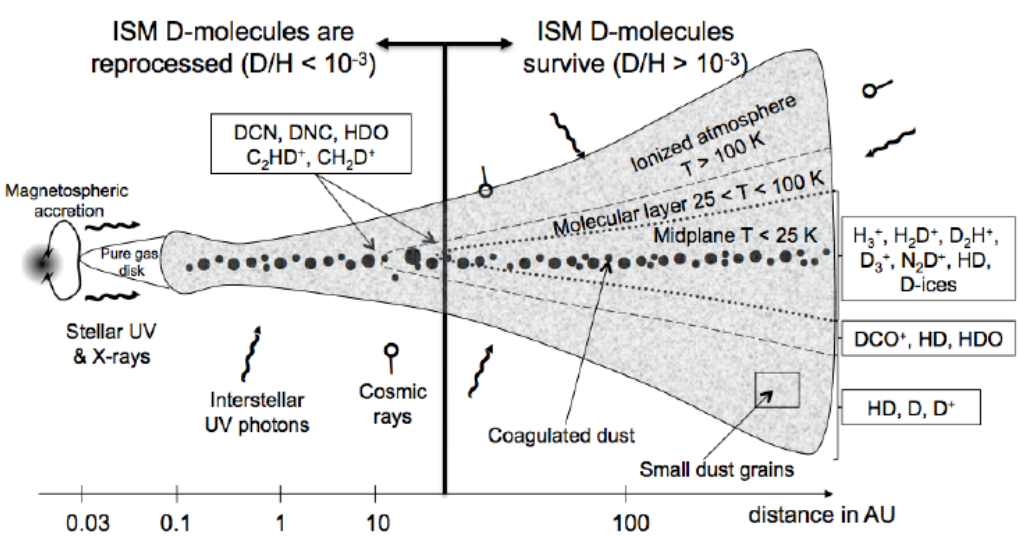

Figure 3: *Schematic vertical cut through a protoplanetary disk around a Sun-like T Tauri star. The disk has a dense cold midplane, where HD gases are formed. Credit: Ceccarelli et al.(2014). [4]*

One method for studying stellar evolution is through observations of protoplanetary disks, such as the one pictured in Figure 3 above. If we can probe disk characteristics such as density, abundance, temperature, thermal history, ionization fraction, evolutionary stage, and chemical composition, we can gain insight to how planetary systems form in the contexts of host stars. This is essential for answering questions on the origins of life in the universe.

Most molecules in the very dense and cold regions of prestellar cores and protoplanetary disk outer midplanes bear heavy elements that freeze onto dust grains, but the lighter molecule of HD remains gaseous and results in deuterating H_3^+ to D_3^+ in a series of barrierless, exoergic isotope-exchange reactions [7]

$$H_3^+ + HD \longrightarrow H_2D^+ + H_2 + 232K, \tag{1}$$

$$H_2D^+ + HD \longrightarrow D_2H^+ + H_2 + 187K, \tag{2}$$

$$D_2H^+ + HD \longrightarrow D_3^+ + H_2 + 234K. \tag{3}$$

At significantly colder temperatures exoergic D-substitution reactions go forward whereas endoergic H-substitution ones do not which can explain observed abundance ratios between the two species, specifically that it is orders of magnitudes above the Big Bang Nucleosynthesis-created galactic D/H ratio of 1.6×10^-5 [11]. Other molecules such as N_2D^+ further drive deuterium fractionation, so we want to understand how H_3^+ and its isotopologues lead to N_2H^+ & N_2D^+.

2.2.2 Tracing Stellar Evolution

The deuterium fractionation ratio of N_2D^+/N_2H^+ provides a chemical age to compare to dynamical models of core formation and evolution, and values imply longer timescales than current models predict for core formation/evolution, possibly explained by the role of magnetic fields [6]. This theory relies on accurate kinetics data, so in the lab we produce N_2H^+ and N_2D^+ via the following chemical reactions

$$N_2 + H_3^+ \longrightarrow N_2H^+ + H_2 \tag{4}$$

$$N_2 + H_2D^+ \longrightarrow N_2H^+ + HD \tag{5}$$

$$N_2 + D_2H^+ \longrightarrow N_2H^+ + D_2 \tag{6}$$

$$N_2 + D_3^+ \longrightarrow N_2D^+ + D_2 \tag{7}$$

$$N_2 + D_2H^+ \longrightarrow N_2D^+ + HD \tag{8}$$

$$N_2 + H_2D^+ \longrightarrow N_2D^+ + H_2 \tag{9}$$

and measure the thermal rate coefficient. Shorter inferred chemical ages and thus inferred role of magnetic fields hinges on k values that are faster. However, the public reaction rate coefficients reviewed by Anich (2003) scatter by a factor of 2 from 1 - 2 $\times 10^{-9} cm^3 s^{-1}$ and measurements do not agree within error (typical uncertainties are 20%). This calls for a need for kinetics data from the

lab, which we plan to generate from our integral cross section (ICS) results, to be incorporated in currently standing astrochemical models and for future developments to compare to observations.

Also, values of k faster than the ones currently used in models would lead to higher tracer densities which impacts our understanding of the structures in protoplanetary disks. Figure 4 below shows declination vs right ascension contour plots from Submillimeter Array (SMA) observations (2008-2012) of the stars TW Hya and HD 163296, their locations indicated by the star symbol, with emission line distributions of H_2CO & N_2H^+ mapped on top, their varying flux intensities shown in a color gradient. Such analyses need to be compared to reliable kinetics data in order to give accurate or meaningful insights to disk characteristics, which are important for stellar and planetary studies.

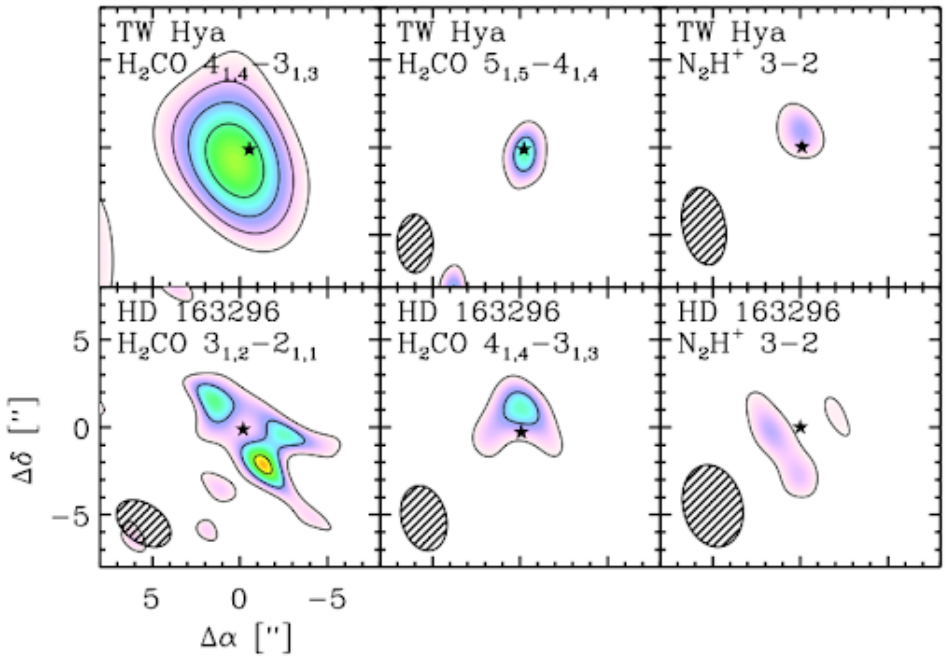

Figure 4: *Submillimeter Array observations (2008-2012) of H_2CO and N_2H^+ emission line distributions in disks of stars TW Hya & HD 163296. The axes are the RA and Dec, the different colors are contour levels, and the star symbol indicates the stellar position. Credit: Qi et al. (2013). [9]*

3 Experimental Details

The methodology of data collection is to use a dual-source, ion-neutral, merged-fast-beam apparatus to make signal count measurements for obtaining k. There are some preparatory work involved to operate the experiment. This section includes details of this as well as of the apparatus and experimental process.

3.1 Apparatus Description

Figure 5 below shows a scheme of the dual-source, ion-neutral, merged-fast-beam apparatus. It was built with support from the NSF Division of Astronomical Sciences (AST) Advanced Technologies and Instrumentation (ATI) Program, through award AST-0905832 for which Dr. Savin was the Principal Investigator (PI). There are four main regions: ion beamline, neutral beamline, interaction region, and detector region. The following sections go over each of these regions.

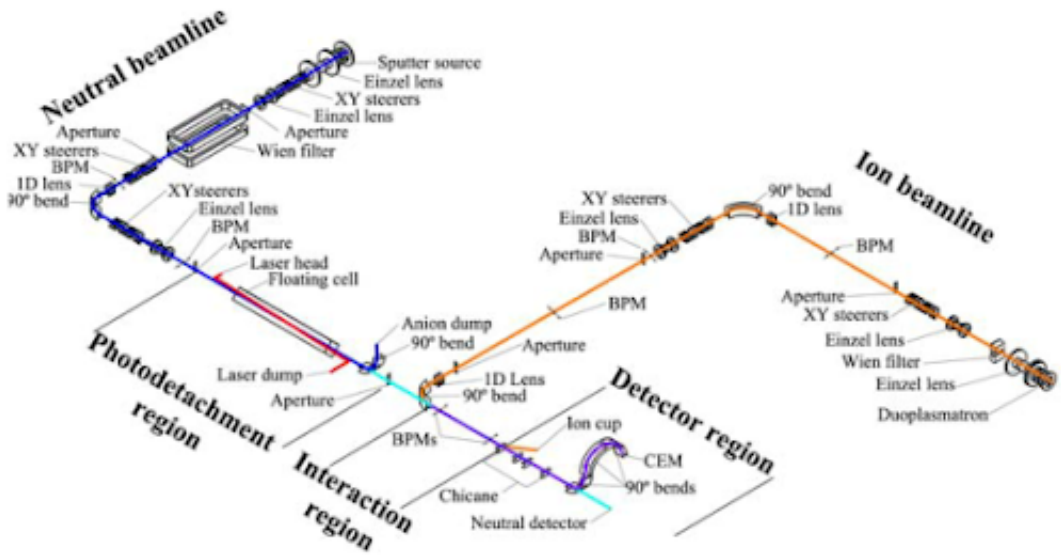

Figure 5: *Schematic of the dual-source, ion-neutral, merged-fast-beam apparatus. The sputter source will be replaced with a duoplasmatron to produce fast beams of N_2^+. The photodetachment region will be used as an N_2 gas cell for electron capture to produce the desired fast N_2 beam. Credit: Savin, D. W. [8]*

3.1.1 Ion Beamline

The ion beams in this experiment are H_3^+ and its isotopologues and have energies about 5 keV associated with them. The ion beam is produced by a duoplasmatron ion source containing mixtures of H_2 or D_2 gases. Through heating an electron emitting cathode or "filament", that is increasing the voltage, we produce high energy electrons at the source which is supplied with molecular gas mixtures. These electrons collide with the gas in a magnetic field and the gas becomes ionized (see Figure 6 below). Then it is moved through an electrode as a beam before being electrostatically filtered to select the desired ion beam [8].

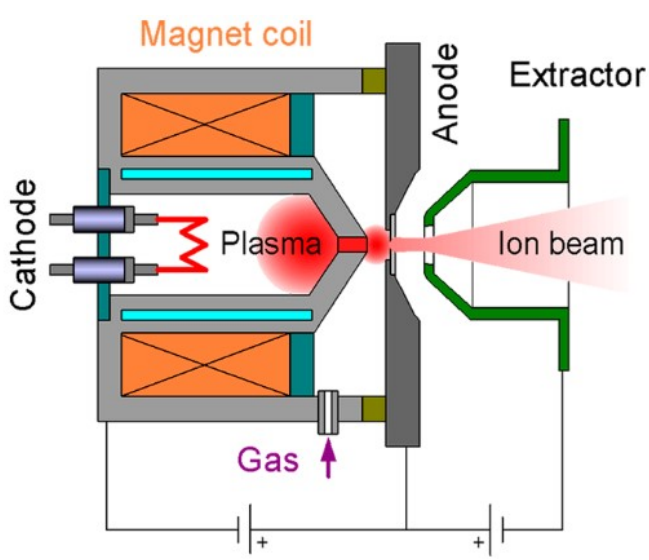

Figure 6: *Diagram of plasma production. Credit: CMAM.*

We select the beams using a Wien filter, pictured in Figure 7 below. A Wien filter uses magnets to separate our H_3^+/H_3^+ isotopologues from other ions produced such as H_2^+, H_2O^+, O_2^+, CO^+, CO_2^+, N^+, etc. based on their differing masses as each will experience unique deflection trajectories, effectively operating as a mass spectrometer.

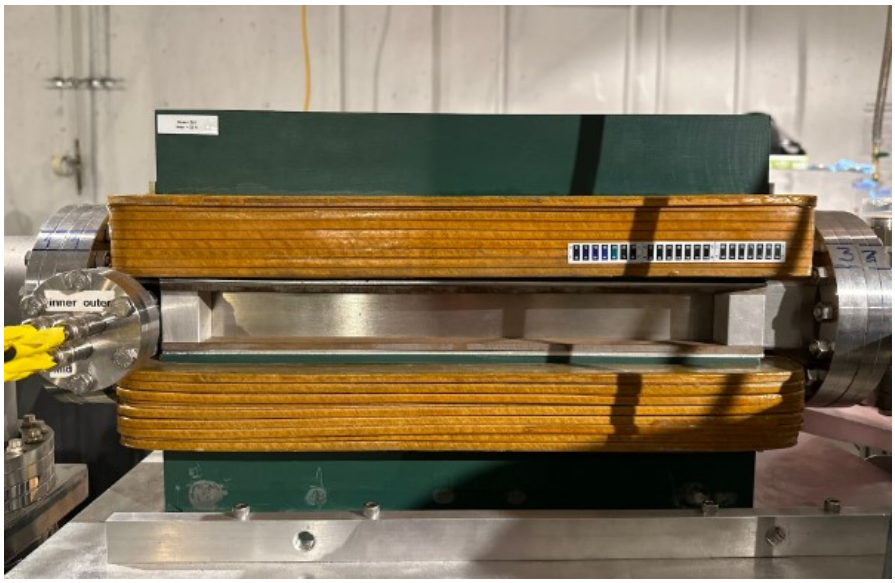

Figure 7: *Image of a Wien filter.*

First we have the Lorentz Force which combines the electric and magnetic forces

$$F = q(E + v \times B) \tag{10}$$

where q is the charge of a particle, E is the electric field, v is the velocity of the particle, and B is the magnetic field. E is given by

$$E = \frac{1}{4\pi\epsilon_0}\frac{q}{r^2} \tag{11}$$

where $\epsilon_0 = 8.854187817 \times 10^{-12} F \cdot m^{-1}$ is the absolute dielectric permittivity of classical vacuum and r is the distance from the charge. B is given by

$$B = \frac{\mu_0}{4\pi}\frac{qv}{r^2} \tag{12}$$

where $\mu_0 = 4\pi \times 10^{-7} N \cdot s^2/C^2$ is the permeability of free space. Then we have Newton's Second Law

$$F = ma \tag{13}$$

where m is the mass of an object and a is its acceleration. Combining Equation (10) with Equation (13) yields

$$(\frac{m}{q})a = E + v \times B \tag{14}$$

which describes the motion of a charged particle in a vacuum, such as the ones we utilize in the laboratory at our Wien filters. Along with the initial conditions of the ions, the trajectory it follows

in the filter is completely dictated by the mass-to-charge ratio, m/q. This is how the filter separates the different ions. This derivation is from Rose (2008) [10].

Using mass-to-charge ratios, our m/q = 3 beams of H_3^+ will be $\lesssim 3\%$ HD^+ and our m/q = 4 beams of H_2D^+ will be $\lesssim 3\%$ D_2^+. Our m/q = 5 D_2H^+ and m/q = 6 D_3^+ beams will be 100% pure.

3.1.2 Neutral Beamline

The neutral beam used in this experiment is fast N_2. We again use the same plasma production as before to first produce a fast ion beam of N_2^+ extracted to a translational lab energy of 20 keV, and separate the desired beam from other products using the same filtering process as before. The fast N_2 beam is produced by sending the fast N_2^+ beam through a gas/"floating" cell (labeled as such in Figure 5 of N_2 at room temperature where near-resonant electron capture occurs via

$$\underline{N_2^+}(X^2\Sigma_g^+) + N_2(X^1\Sigma_g^+) \longrightarrow \underline{N_2}(X^1\Sigma_g^+) + N_2^+(X^2\Sigma_g^+) \tag{15}$$

where the underline above indicates the fast particle and $X^1\Sigma_g^+$ is the ground electronic state. The fast neutral beam then continues on ballistically towards the interaction region and remaining fast cations are electrostatically removed after the gas cell exit.

3.1.3 Interaction Region

In the interaction region, the two 5-mm diameter beams are merged onto each other and interact for a distance of L $\approx$ 120 cm in the single-collision regime. They co-propagate at keV/u energies and we can achieve relative collision energies, E_r, from 2 meV to 20 eV. The result, using 0.714 keV/amu beams as an example, is the exoergic reaction

$$N_2(20keV) + H_3^+(2.142keV) \longrightarrow N_2H^+(20.714keV) + H_2(1.428keV). \tag{16}$$

There are two measurements made in this region: ion and neutral currents. The ion currents are measured using a Faraday Cup and a static cup in the chicane, and the neutral currents are measured using a calibrated neutral detector.

Neutral detection is enabled by the fast neutral beam hitting an electron emitting target, so that when the beam is incident on this plate, electrons are collected and measured. This electronic signal, measured as a current in nA, is converted to a neutral current signal via [8]

$$I_n = \frac{I_{ND}}{\gamma T_n} \tag{17}$$

where I_{ND} is the current measured on the neutral detector, γ is the secondary negative particle emission coefficient, and T_n is a transmission efficiency factor of the neutral beam entering the interaction region to the neutral detector which is ideally 1.0 but in practice around $\gtrsim 0.9$. γ is given by

$$\gamma = \frac{I(N_2)_{fin}}{I(N_2^+)_{UCD} - I(N_2^+)_{UCD}^{gas}} \cdot \frac{I(N_2^+)_{UCD}}{I(N_2^+)_{fin}} \tag{18}$$

where "fin" refers to a current measurement at the final analyzer, "UCD" refers to the upper cup, and "gas" implies the measurement occurs when the beamline has been supplied with N_2 gas. Our recent measurement of $\gamma = 1.81 \pm 0.01$. T_n is given by

$$T_n = \frac{I(N_2^+)_{fin}}{I(N_2^+)_{int}} \tag{19}$$

where "int" refers to the interaction region. Our recent measurement of $T_n = 1.00$, which is ideal. There is also an additional measurement made T_i which is the transmission efficieny factor of the ion beam entering the interaction region to the ion detector which is ideally 1.00 but our recent measurement is $T_i = 0.93$. T_i is given by

$$T_i = \frac{I(D_3^+)_{chicane}}{I(D_3^+)_{FCC}} \tag{20}$$

where "chicane" refers to, as the name suggests, the chicane and "FCC" refers to Faraday Cup C.

3.1.4 Detector Region

Once the beams are merged and pass through the interaction region, the ion products are electrostatically moved upwards into the detector region and selected for measurement. Experimentally we measure the ICS σ times the relative velocity, v_r averaged over the energy spread of the merged beams, $< \sigma v_r >$. This merged-beams rate coefficient can be written as [8]

$$< \sigma v_r >= \frac{S}{T_a T_g \eta} \frac{e^2}{I_n I_i} \frac{v_n v_i}{L < \Omega(z) >}. \tag{21}$$

Here S is the count rate measured at the channel electron multiplier (CEM) and is roughly 24 keV, T_a is the transmittance of the analyzer for the selected daughter product, T_g is the geometric transmittance of the grid in front of the CEM, η is the CEM efficiency (all ideally 1.00), v_n is the neutral beam velocity, v_i is that of the ion beam (extracted from lab energies of 23 keV and 5 keV, respectively), I_n is the neutral particle current measured in amperes, I_i is the ion current (both typically in the 100s of nA), L is the length of the interaction region of 1.2 m, and $<\Omega(z)>$ is the average overlap integral in the interaction region along the propagation axis, z. The overlap between the two beams at an arbitrary position is given by [8]

$$\Omega(z) = \frac{\iint J_n(x,y,z) J_i(x,y,z) dxdy}{\iint J_n(x,y,z) dxdy \iint J_i(x,y,z) dxdy} \tag{22}$$

where Jn and Ji are the fluxes of the neutral and ion beams, respectively, z is as described above, and x and y are both perpendicular to the z axis and to one another. Bruhns et al. (2010b) [3] explains how to extract the average overlap factor in the interaction region using beam profile monitor (BPM) data in a Monte Carlo trajectory simulation via [8]

$$< \Omega(z) >= \frac{1}{L} \int_0^L \Omega(z) dz. \tag{23}$$

Equation 21 enables us to deconvolve our results to generate cross sections by dividing out v_r giving

$$\sigma = \frac{\sigma v_r}{v_r} \tag{24}$$

which can then be re-convolved with a Maxwell–Boltzmann distribution to generate a translational temperature rate coefficient.

3.2 Experimental Steps

In order to run the experiment itself, there are six main steps: (1) cooling the system, (2) heating the filaments for ion production, (3) refreshing gas lines, (4) enabling and optimizing ion optics, (5) checking interaction region beam profiles, and (6) taking measurements.

Referring back to Figure 5, after ion production in the Peabody duoplasmatron sources and extraction/selection in the Wien filters, the beams go through a series of ion optic apertures: Einzel lenses, XY steerers, 1D lenses, 90° bends, Chicane, kicker, and chopper; and tools: Faraday cups (FCs) and beam profile monitors (BPMs), which are described in Bruhns et al. (2010b) [3].

An Einzel lens is essentially a tube with a symmetric electric potential across it to focus the beam without changing its energy. The lens is made up of cylindrical walls in series with voltages applied to them. Varying the voltages from one another causes the gaps to function as a lens. The change in radial velocity for a charged particle as it passes between any pair of cylinders in the lens is [1]

$$\Delta v_r = \int \frac{qE_r(r,z)}{mv_z} dz, \tag{25}$$

with the z axis being defined as passing through the middle of the lens and r being the direction normal to z, q being the charge of the particle, m as its mass, v_z its velocity along z, and E_r(r,z) is the magnitude of the electric field in the radial direction for a particle at a particular radial distance (r) and distance across the gap (z). The bounds of the integral are over the gap between the plates, where the lensing occurs.

XY steerers follow similar mechanisms but for a series of four alternating pairs of parallel plates which steer in the horizontal (X) and vertical (Y) directions. Likewise, 1D lenses, which are made of two plates, are used before the bends for beam diffraction. The 90 ° bends are two curved plates where the inside and outside plate have different signed charges so as to move the ion beam along the path curvature with a radius of 150 mm. Also, a "kicker" is installed at the entrance of the interaction region to vertically shift the beam with one plate. Here there is also a "chopper" or electrostatic gate that turns beam-beam interaction on/off.

Lastly, throughout the paper there has been mention of taking measurements with FCs and BPMs. An FC controls ion intensity and is used to measure currents. It is a metal cup that collects particles in vacuo and current measurements are determined by the amount and location that ions hit the metal surface. Their charges are transferred to the wall which is apart of a circuit and the number of ions, N, hitting the cup per unit time, t, is given by [2]

$$\frac{N}{t} = \frac{I}{e} \tag{26}$$

where I is the current and e is the elementary charge of an electron, thus giving a reliable and direct relationship between he measured current and number of ions.

A BPM is a rotating wire that registrates the beam as ions heat it, giving the position and amount of them. In the experiment we analyze the vertical and horizontal cross sections at two locations around the interaction region, given by BPM 3 and BPM 4, to ensure N_2H^+ (or N_2D^+) production. An example of beam-beam overlapping is shown in Figure 8 Here there are four plots generated, a pair of vertical and horizontal areas for each location, where the neutral beam is outline in purple, the ion beam in blue, and the region of overlap is shaded in green (orange indicates non-overlap). Vertical BPM 3 is showing good overlap with the best overlap to non-overlap ratio (the green area is much larger than the orange), that is both profiles are gaussian in shape, with aligned centers as indicated by the single vertical line, and matching focuses. You can see this is not the case in Vertical BPM 4 where they are no longer perfectly gaussian, there is some skewness or tail at the

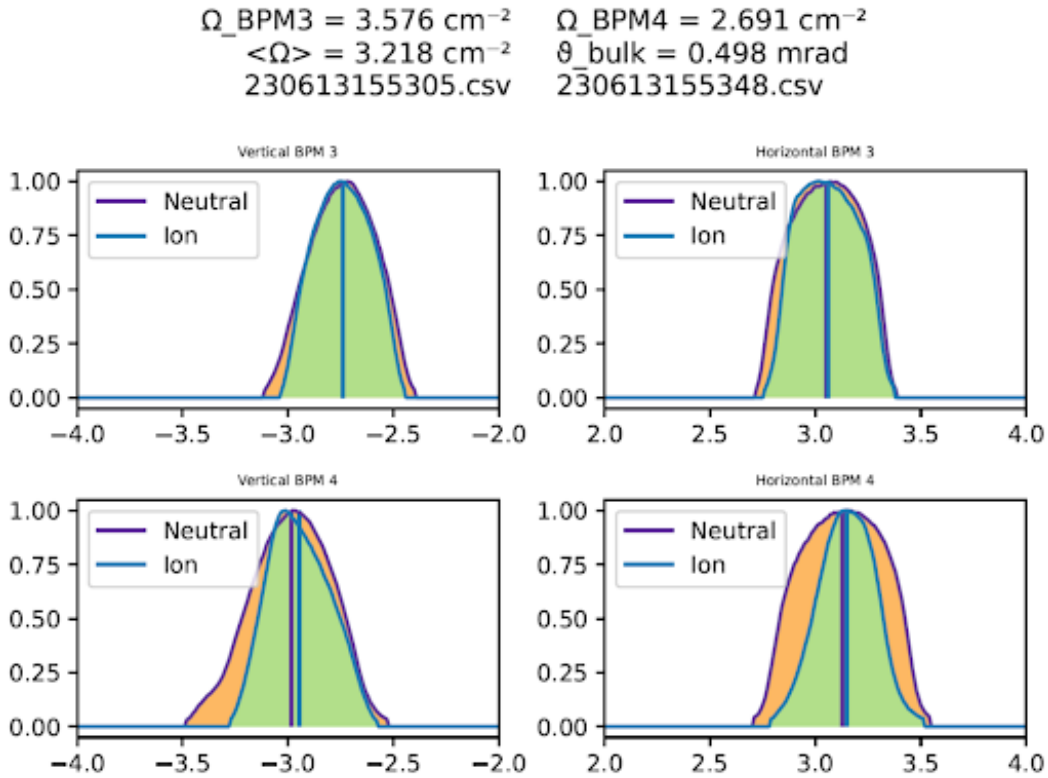

Figure 8: *Beam Profile Data Plots generated by Dr. Dmitry Ivanov in The Savin Group.*

tapering off causing greater amounts of non-overlap comparatively, and their centers are misaligned as indicated by the double purple and blue vertical lines. Horizontal BPM 4 also shows how the beams can differ in focus as the ion beam here is displayed as being more focused than the neutral beam, or the neutral beam is more defocused than the ion beam, that is their widths are narrower or wider, respectively, resulting in a larger orange non-overlap region. Despite these imperfections, the overlap area is 3.218 cm^{-2} which is more than adequate for daughter ion production.

Other measurements made in the lab are the positions of the BPMs and the distances between them which are used in the overlap measurement, fractionation which is the effectiveness of neutralization and reionization used in γ factor measurements, floating cell shift which is the difference in voltage in the kV range between real equipment and the computer program (LABVIEW), channeltron efficiency which is based on the fraction of ions present to detected, and neutral and ion amplifications or the sensitivities on our Keithley instruments.

3.3 Preparation

In order to operate the apparatus, there was some preparatory work involved such as stand modification, mounting a high vacuum system to the stand, taking inventory of turbomolecular vacuum pumps, N_2 leak detection, tracing carbon monoxide (CO) exhaust lines, and considering CO safety. These items will be discussed in further detail in the following section.

4 Results

In this section I go over the various accomplishments during this summer program. They are hardware-related tasks and lab measurements with subsequent analyses from experimental runs.

4.1 Hardware Deliverables

Figure 9: *Metal stand before modifications.*

One of the first things I did was modify a stand (see Figure 9). This would be used for hosting a vacuum system so I measured dimensions, created a schematic of what it should look like, made changes to the structure, mounted the vacuum system, and found a location in the lab to place it.

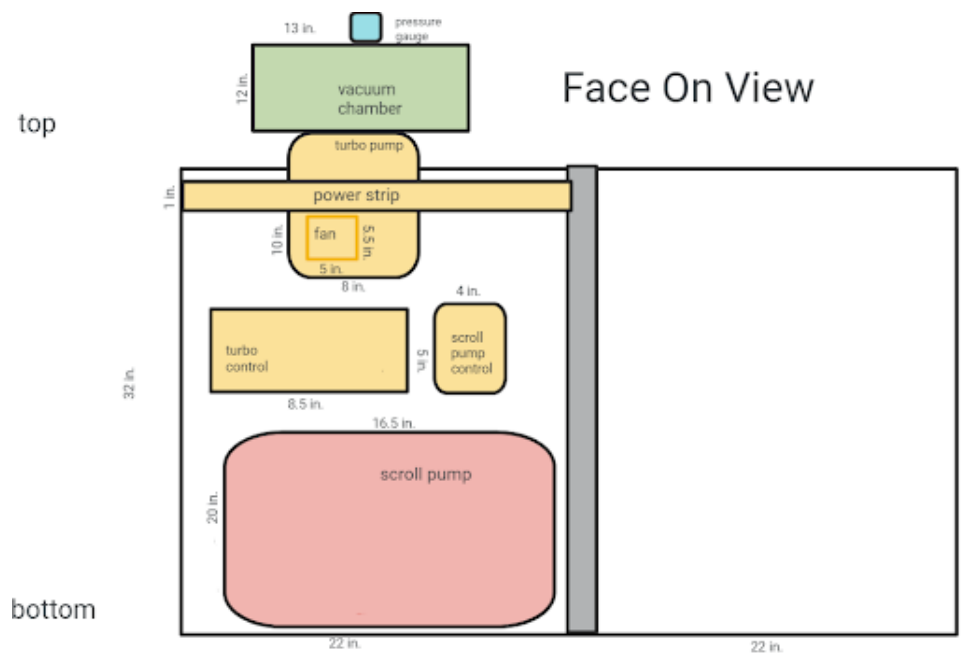

Figure 10: *Face on view schematic of the stand hosting a vacuum system.*

Figure 10 is a depiction of what the end result would be. There are various pieces in this schematic; a vacuum chamber and pump with a fan of course, as well as a supplementary scroll pump, their pressure gauges and control units, and a power strip for all the electronics. Notice that the entire system fits on one half of the stand, allowing for future installations.

Figure 11: *Metal stand after modifications and with a vacuum system mounted, including a channeltron.*

Lastly, Figure 11 shows the final result. You will notice there is an additional part connected to the chamber. This is the channeltron, a device at the detector region of the apparatus. This region underwent an extension, and due to the sensitivity of the channeltron, we created this vacuum system to prevent exposure to atmosphere.

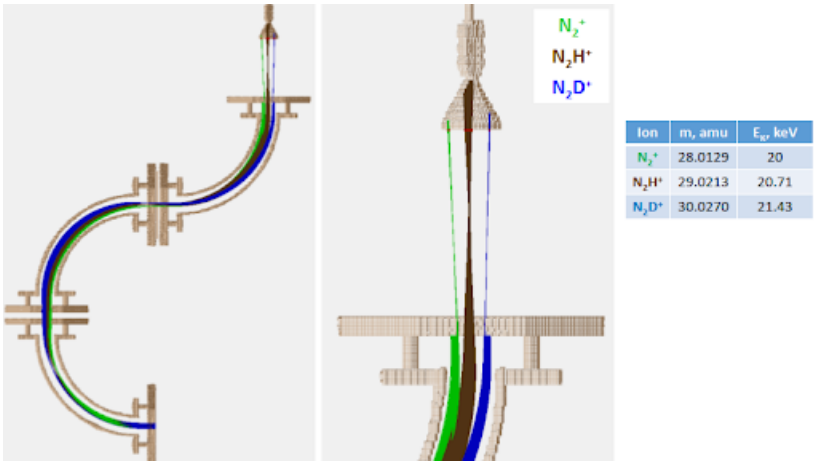

Ion	m, amu	E_{ip}, keV
N_2^+	28.0129	20
N_2H^+	29.0213	20.71
N_2D^+	30.0270	21.43

Figure 12: *SIMION simulation of ion beams before installation of a nipple to extend the detector region. Masses of the product beams are displayed in a table. Credit: Dr. Dmitry Ivanov.*

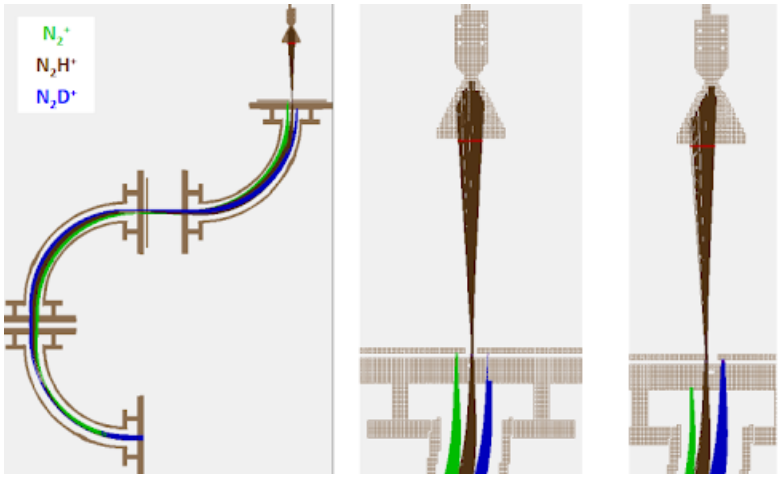

Figure 13: *SIMION simulation of ion beams after installation of a nipple to extend the detector region. Focal length has changed and a slit can be inserted for better product selection at the focal point. Credit: Dr. Dmitry Ivanov.*

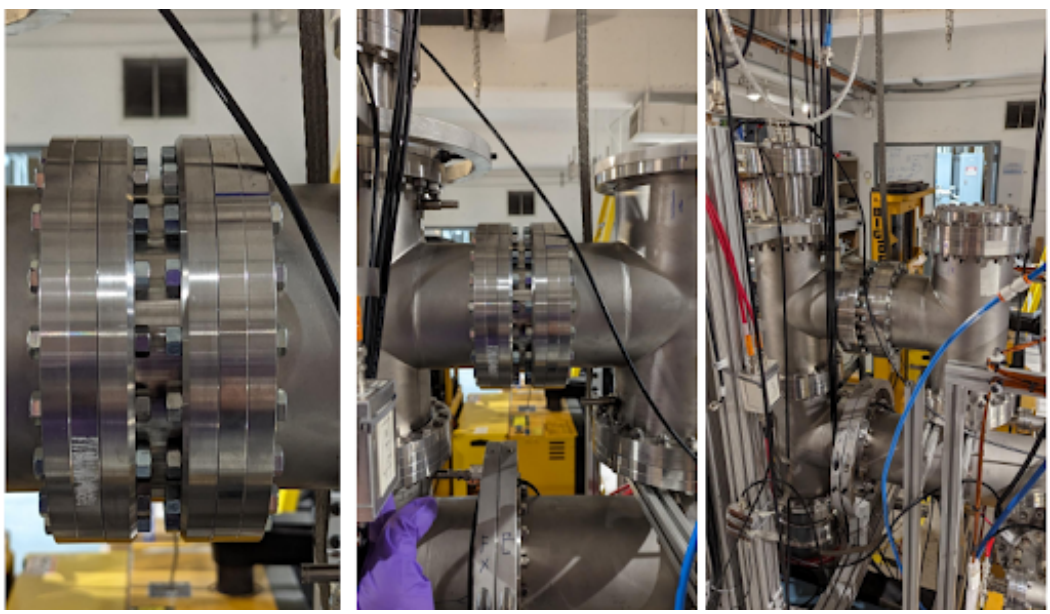

Figure 14: *Nipple installation to extend detector region.*

The extension at the detector region, or installation of a nipple, was necessary for better experimental results. It was difficult before to separate product beams from one another as they are similar in masses (see Figure 12). Simulations in SIMION (see Figure 13) show that with an extension, the change in the focal length of the product beams allows a slit to be inserted at the focal point so that we are able to select/separate the products more easily. The extension, accomplished by Dr. Dmitry Ivanov and Dr. Daniel Wolf Savin, is shown in Figure 14.

Another necessity for the lab is the tracing of scroll pump exhaust lines to ensure their gas is exiting the lab through a proper ventilation system. This is done in preparation for utilizing CO in a future experiment that reacts CO with H_3^+. Figure 15 shows the various scroll pumps in the lab, their location, connections, and the vent (the gray rectangle that connections go to. Notice that scroll pumps B and 3 are connected to each other, I had to do this as well as then connect scroll pump B to the vent (see Figure 16). It turns out that this vent actually does not exit the lab.

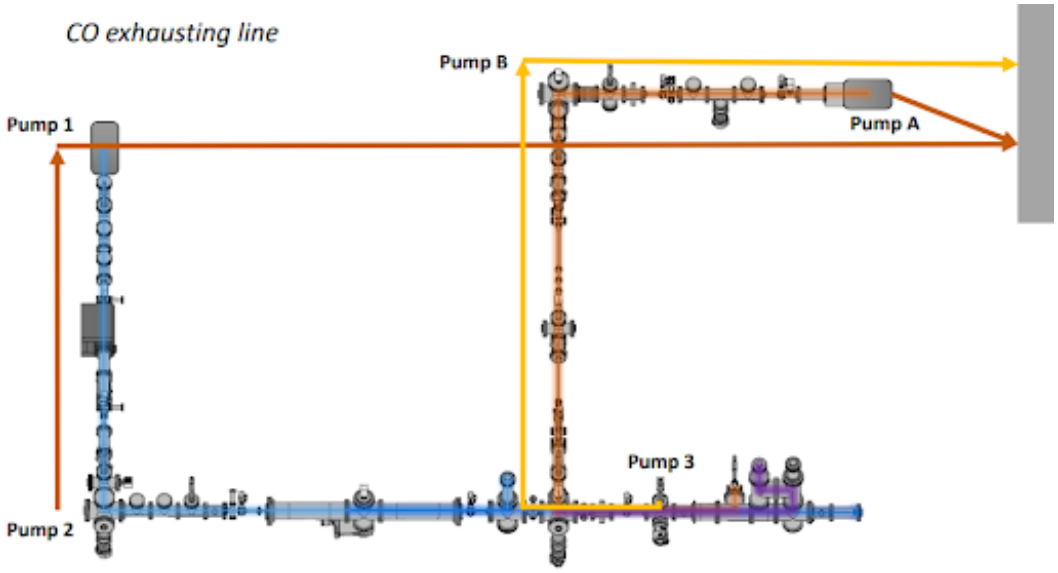

Figure 15: *CO scroll pump exhaust lines schematic. credit: Dr. Dmitry Ivanov.*

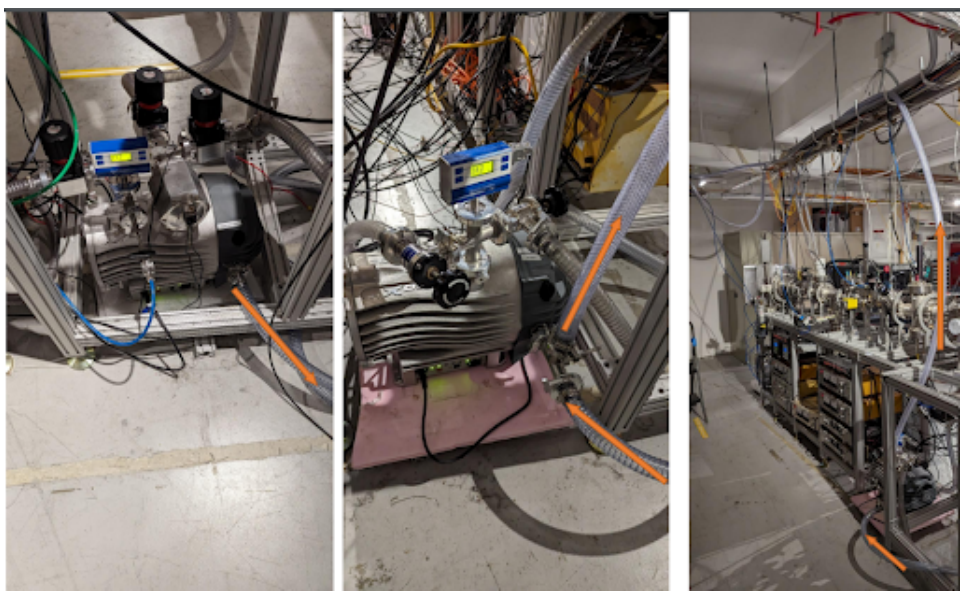

Figure 16: *Connections of scroll pumps 3 to scroll pump B and then to the vent.*

Also on CO safety in the lab, on July 27th, we met with Columbia University's Environmental Health & Safety.The following is a list of requirements to implement in the lab:

1. Gas cabinet at source location to contain CO
2. CO detector above gas cabinet for leakage alerts
3. Steel lines to move gas i.e. through the apparatus and exhaust lines
4. Flash arrestors at gas cylinders to stop flames and reverse gas flow
5. Signage at entrances to indicate CO usage and hazards
6. Training courses for operating CO

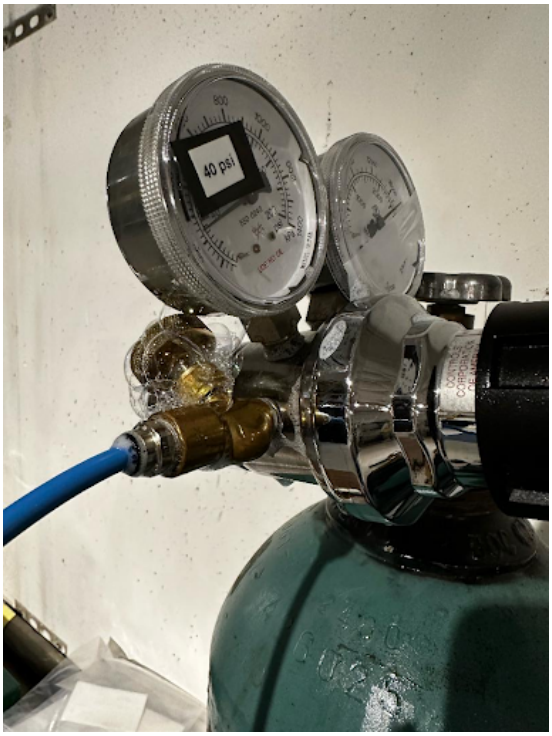

Figure 17: *N_2 leak, indicated by bubbles, detected at cylinder valve using a liquid leak detection solution.*

These items are obligatory for CO usage in the lab, and most deal with leak prevention i.e. the cabinet, detector, steel lines, and flash arrestors. This is especially critical in our lab as there is a current gas leak of N_2. Although this gas is natural and not hazardous, it is still of concern and a priority to fix the leak.

I actually worked with Dr. Dmitry Ivanov to detect and fix the leakage. We tried four methods: pump out and degas the entire apparatus in sections to compare pressures to indicate a more specific location where the leak may possibly reside, for the same purpose then to also supply the sections with gas and check pressure over time to identify sudden drops, manually check each connection and tighten them, use a liquid leak detection solution on connections and the line. Of the four methods, we successfully located one source of a leak using the liquid solution. There was a loose valve at the cylinder which shows a leak indicated by the bubbles formed when applying the solution at the connection (see Figure 17).

More housekeeping involved taking inventory of all the turbomolecular vacuum pumps and checking their statuses. The following table shows the pumps labeled by their unofficial names in the lab, their official make/model, the number of hours they have been operating since last being sent to service/all time if they have not yet done so, current in Amperes which is also an indicator of whether or not they need to be sent in for maintenance, pressure in torr, and which region of the apparatus they reside in (the Hudson line is referring to the neutral beam line and the Broadway line is referring to the ion beam line). There is also a secondary table of spare pumps.

Lastly, I helped recoat the filaments (electron emitting cathodes) for both plasma sources to help ion production. They are coated in a mixture of Barium-Strontium-Calcium which will help with thermionic emission. The time between the last coating and this one had been 360 hours of operation. Pictured in Figures 20 and 21 is a before and after.

Name	Model	Operating Hours	Current (A)	Pressure (torr)	Region
Neutral Source	HiPace 300	45135	0.62 +/- 0.03	3.00E-08	Hudson Line
2	HiPace 300	4497	0.37 +/- 0.04	2.00E-08	
3	HiPace 300	3199	0.40 +/- 0.02	3.00E-08	
4	TMU 521 P	87731	0.30 +/- 0.02	1.00E-05	
Dump	HiPace 350	2785	0.25	7.00E-08	
Merger/5	TC 110	397	0.40 +/- 0.05	5.00E-09	Interaction/Detection
Interaction/6	HiPace 300	2797	0.40 +/- 0.04	1.00E-08 ?	
Final Analyzer/7	TV 551	51555	0.8	1.00E-08 ?	
Ion Source	HiPace 300 ?	14694	0.43	8.00E-06	Broadway Line
A	HiPace 300	32768	0.46 +/- 0.02	N/A	
B	HiPace 300	32768	0.18 +/- 0.03	2.00E-08	
C	HiPace 300	2796	0.40 +/- 0.05	1.50E-08	

Figure 18: *Turbomolecular Vacuum Pump List.*

Name	Model	Comments
Spare 1	HiPace 300	Works, located in back room on a wooden board
Spare 2	HiPace 350	New (still in package)
Vacuum Stand Turbo	TV 551	Mounted on stand
Spare 3	TV 551	In appparatus room on table by door

Figure 19: *Spare Turbomolecular Vacuum Pump List.*

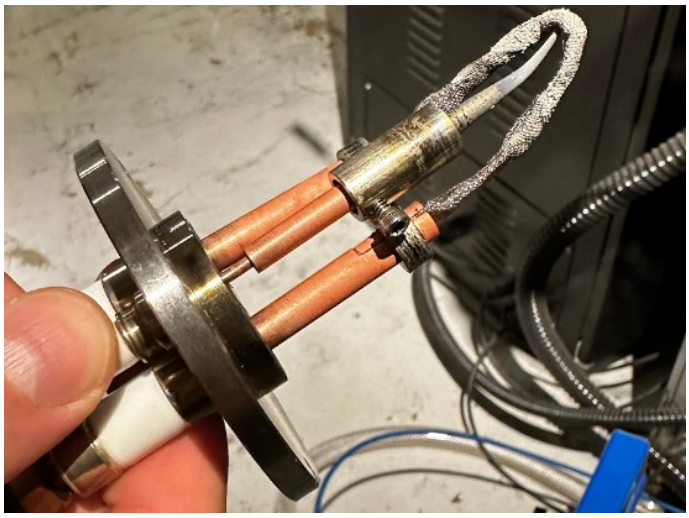

Figure 20: *Filament before coating.*

Figure 21: *Filament after coating.*

4.2 Measurements & Analysis

It was mentioned before that measurements in the lab were of the beam overlapping factor, Ω(z), from BPM 3 and BPM 4 data; the secondary negative particle emission coefficient, γ, from measurements of current at the final analyzer and UCD; and the neutral and ion transmission efficiency factors, T_n and T_i respectively, from measurements of current at the final analyzer, interaction region detector, chicane, and FCC. From our measurements we gather $\gamma = 1.81 \pm 0.01$, $T_n = 1.00$, and $T_i = 0.93$.

Finally we can discuss the final results of the experiment. Figures 22, 23, and 25 show $<\sigma v_r>$ or the merged-beams rate coefficient which is the ICS (σ) times the relative velocity (v_r) averaged over the energy spread of the merged beams in the order of $10^{-10} cm^3 s^{-1}$ versus E_r which is the relative collision energies of the beam in the order of eV on a log scale from experimental runs conducted in June, July, and the combined data weighted averages, respectively, for the reaction of N_2 with D_3^+. Additionally, Figure 22 shows three experimental runs in the month of June conducted on the 12th, 13th, and 14th in green, purple, and blue, for initial ion beam energies of 20, 21, and 20 keV, respectively. Figure 23 which was analyzed on July 7th also shows data for a 20 keV run where the velocity for the neutral beam, v_n, is greater than or equal to the velocity for the ion beam, v_i, in yellow as well as $v_n < v_i$ in red. Lastly, figure 25 shows the weighted averages of all data collected this summer labeled with energy thresholds (2), (3), and (5), which correspond to the reactions and E_r or $-\delta E$ values in the table pictured in figure 24. The plots all show a decreasing signal because competitive reaction channels generate other products and higher excitation levels. Ultimately, the y-axes on these plots as discussed before can be integrated over a Maxwell-Boltzmann distribution to obtain the thermal rate coefficients, k.

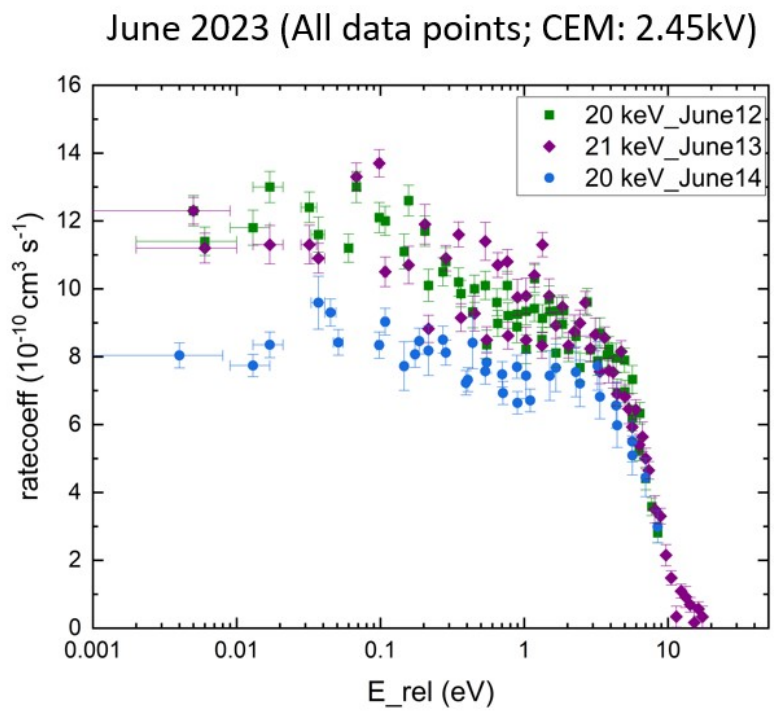

Figure 22: *N_2 reacting with D_3^+ kinetics plot for three experimental runs in the month of June conducted on the 12th, 13th, and 14th for initial ion beam energies of 20, 21, and 20 keV, respectively. Credit: Dr. Dmitry Ivanov.*

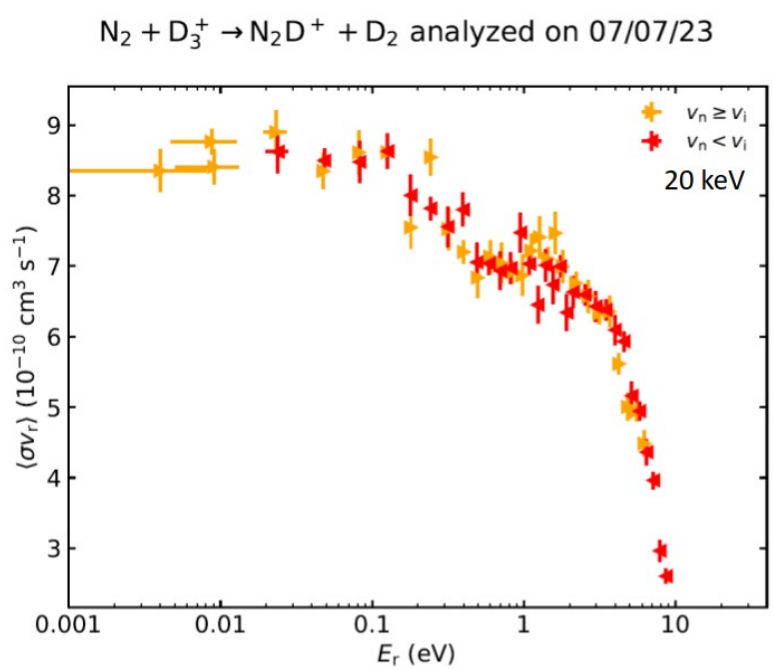

Figure 23: *N_2 reacting with D_3^+ kinetics plot for an experimental run on July 7th for an initial ion beam energy of 20 keV with both $v_n \gtrsim v_i$ and $v_n < v_i$. Credit: Dr. Dmitry Ivanov.*

	$N_2(v = 0) + H_3^+ \rightarrow$	$-\Delta E$, eV
(1)	$N_2H^+ + H_2$	-0.74
(2)	$\mathbf{N_2(v = 1) + H_3^+}$	**0.29**
(3)	$\mathbf{N_2H_2^+ + H}$	**2.42**
(4)	$N_2H^+ + H + H$	3.74
(5)	$\mathbf{N_2 + H_2 + H^+}$	**4.38**
(6)	$N_2 + H_2^+ + H$	6.20
(7)	$N_2^+ + H_2 + H$	6.36
(8)	$N_2 + H + H + H^+$	8.85
(9)	$N + N + H + H + H^+$	18.61

Figure 24: *Table of energy thresholds for various excitation levels of N_2 reacting with D_3^+. Credit: Dr. Dmitry Ivanov.*

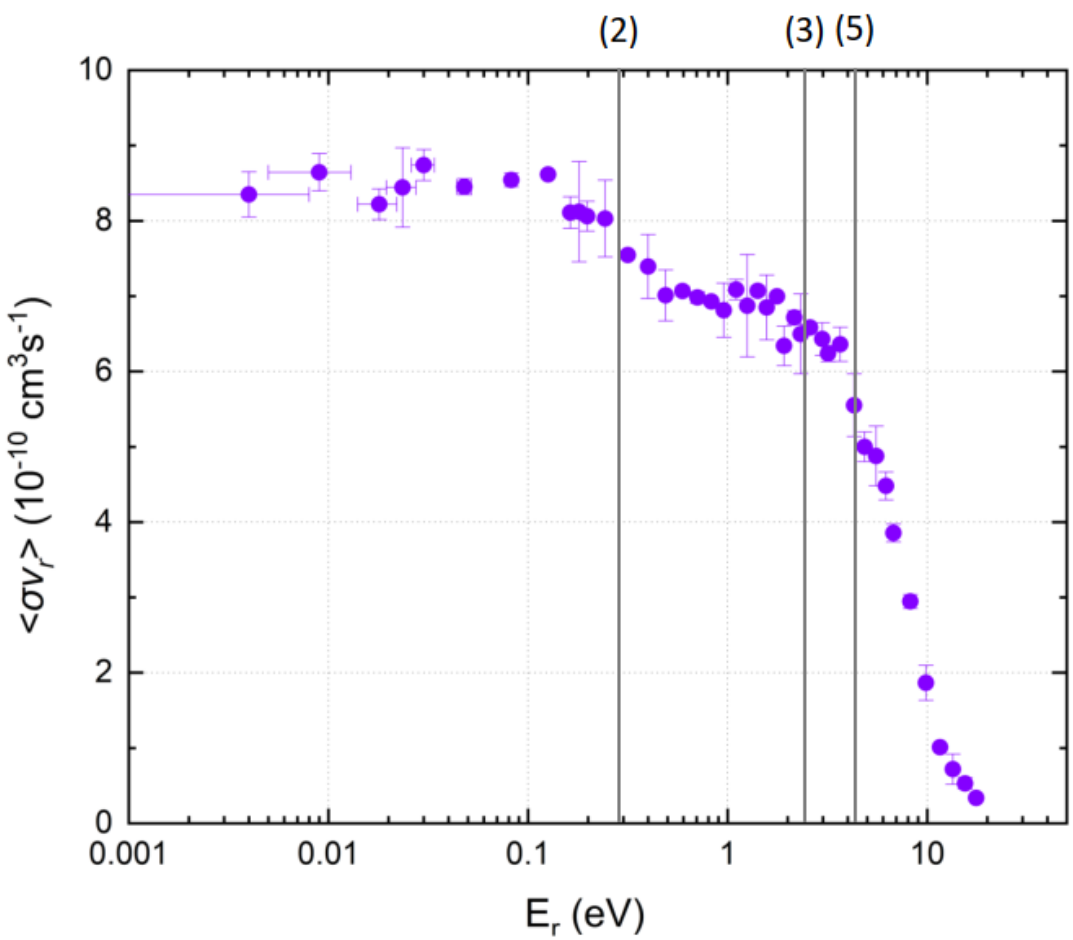

Figure 25: *N_2 reacting with D_3^+ weighted average kinetics plot for all summer experimental runs with energy thresholds corresponding to the table in Figure 24 labeled. Credit: Dr. Dmitry Ivanov.*

5 Conclusion

This concludes the summer project and my role in the lab. The following goes over future steps and the educational merit gained from this research.

5.1 Future Steps

The bulk of remaining steps to take for this research are related to the hardware deliverables. The stand is fixed and the vacuum system functions, operating at $5 \times 10^{-8} torr$, to pump out the channeltron and minimize exposure to air which is currently attached at the chamber. The installation of the nipple to extend the detector region focal length and of the slit at the new focal point for better ion product selection has been completed. With these two in conjunction, the coming weeks will entail having the group detach the channeltron from the vacuum system and reattach it to the detector region. The stand can also host other systems in the future as the right hand side is empty or be extended and/or moved elsewhere as needed. It was also touched upon that the current CO exhaust lines need to be replaced with steel lines and that they do not connect to a real ventilation unit. The lab will have to not only remedy this but also implement the other safety requirements; they need to build a gas cabinet at the source location, install a detector above it, obtain flash arrestors to attach to the cylinders, place hazard signs at the entrances to the lab, and train members that will be using CO directly. Also, the leak is not entirely fixed. It is true that we found one source of a leak in the N_2 line, and that the cylinder tank lasts for over a month now rather than previously lasting only for two weeks, but there may still be leaks present in the line itself that must be addressed. As a note, the lab will need to continuously replace cylinders frequently until this issue is resolved. The same is true for recoating the filaments periodically, typically 360 hours between each subsequent coat. Also, the inventory list shows at least three pumps which are in need of maintenance. These pumps will have to be removed, replaced temporarily, serviced, and re-installed. They are pumps "neutral source", 4, and "final analyzer"/7 indicated by their high operating hours and/or currents of 45135 h and 0.62 ± 0.03 A, 87731 h, and 51555 h and 0.8 A, respectively. That is it for the hardware. Lastly, of course the experimental runs will continue for other initial energies and reactions.

5.2 Educational Merit

This REU program and research project have taught me a multitude of skills. To name them off I was first trained on Responsible Conduct of Research (RCR). Then I went through a learning tutorial for the basics of ROOT and ROOT C++. This was my first time conducting experimental research and doing work that involved hardware. From this I gained insight to interdisciplinary work as I was studying astrochemistry as a physicist by doing engineering-type tasks.

6 Acknowledgements

This material is based upon work supported by the National Science Foundation under Grant No. PHY/1950431. I would like to thank the Columbia University Nevis Laboratories REU program for this research opportunity, in particular the program heads, Georgia Karagiorgi and John Parsons. I would also like to thank my PI, Dr. Daniel W. Savin, and laboratory mentor, Dr. Dmitry Ivanov, for their guidance.

References

[1] William H. Aberth, Rafael Schnitzer, and Ferdinand C. Engesser. Construction of an einzel lens capable of high voltage operation. *Review of Scientific Instruments*, 45(10):1289–1290, 11 2003.

[2] K. L. Brown and G. W. Tautfest. Faradayâ€Cup Monitors for Highâ€Energy Electron Beams. *Review of Scientific Instruments*, 27(9):696–702, 12 2004.

[3] H. Bruhns, H. Kreckel, K. A. Miller, X. Urbain, and D. W. Savin. Absolute energy-resolved measurements of the $H^-+H \rightarrow H_2+e^-$ associative detachment reaction using a merged-beam apparatus. , 82(4):042708, October 2010.

[4] C. Ceccarelli, P. Caselli, D. Bockelée-Morvan, O. Mousis, S. Pizzarello, F. Robert, and D. Semenov. Deuterium Fractionation: The Ariadne's Thread from the Precollapse Phase to Meteorites and Comets Today. In Henrik Beuther, Ralf S. Klessen, Cornelis P. Dullemond, and Thomas Henning, editors, *Protostars and Planets VI*, pages 859–882, January 2014.

[5] Gaia Collaboration. Gaia data release 2 - observational hertzsprung-russell diagrams. *A&A*, 616:A10, 2018.

[6] Shuo Kong, Paola Caselli, Jonathan C. Tan, Valentine Wakelam, and Olli Sipilä. The Deuterium Fractionation Timescale in Dense Cloud Cores: A Parameter Space Exploration. , 804(2):98, May 2015.

[7] Kristensen, L. E., Amiaud, L., Fillion, J.-H., Dulieu, F., and Lemaire, J.-L. H2, hd, and d2 abundances on ice-covered dust grains in dark clouds. *A&A*, 527:A44, 2011.

[8] A. P. O'Connor, X. Urbain, J. Stützel, K. A. Miller, N. de Ruette, M. Garrido, and D. W. Savin. Reaction studies of neutral atomic c with using a merged-beams apparatus. *The Astrophysical Journal Supplement Series*, 219(1):6, jul 2015.

[9] Chunhua Qi, Karin I. Öberg, and David J. Wilner. H2co and n2h+ in protoplanetary disks: Evidence for a co-ice regulated chemistry. *The Astrophysical Journal*, 765(1):34, feb 2013.

[10] H H Rose. Optics of high-performance electron microscopes*. *Science and Technology of Advanced Materials*, 9(1):014107, apr 2008.

[11] M. Tanabashi. Review of particle physics. *Phys. Rev. D*, 98:030001, Aug 2018.

[12] Kastytis Zubovas, Kostas Sabulis, and Rokas Naujalis. Collapse and fragmentation of molecular clouds under pressure. *Monthly Notices of the Royal Astronomical Society*, 442(3):2837–2854, 06 2014.